LA-UR- 01-3080

*Approved for public release; distribution is unlimited.*

*Title:* Residual Stresses in Continuous Tungsten Fiber Reinforced Kanthal Matrix Composites

*Author(s):* Partha Rangaswamy, MST-8
Irene J. Beyerlein, MST-8
Mark A. M. Bourke, MST-8
Michael B. Prime, ESA-EA
Anil K. Saigal, Tufts University
Todd O. Williams, T3

*Submitted to:* Philosophical Magazine A



Rangaswamy, P., Beyerlein, I. J., Bourke, M. A. M., Prime, M. B., Saigal, A. K., and Williams, T. O., 2003, "Residual stresses in continuous-tungsten-fibre-reinforced Kanthal-matrix composites," Philosophical Magazine, **83**(19), pp. 2267-2292.

# Residual Stresses in Continuous Tungsten Fiber Reinforced Kanthal Matrix Composites

*P. Rangaswamy [1], I. J. Beyerlein [1], M.A.M. Bourke [1], M. B. Prime [1], A. K. Saigal [2], T. O.Williams [1]

[1]Los Alamos National Laboratory
Los Alamos, NM 87545

[2]Tufts University
Medford, MA 02155

*email: partha@lanl.gov

# ABSTRACT

Residual stresses were measured in four (10%, 20%, 30%, and 70% tungsten) Kanthal matrix – continuous tungsten fiber composites using neutron diffraction. Parallel to the fibers the stress in the Kanthal ranged from 40 (10 %) to 1100 (70 %) MPa compared to -1877 (10 %) to -400 (70 %) for the tungsten. Perpendicular to the fibers the stress ranged from -52 (10%) to 620 (70%) in the Kanthal compared to -778 (10%) to -195 (70%) in the tungsten. Predictions, assuming the measured residual stresses were solely thermal in origin, were made using concentric cylinder and finite element models. In the absence of hardening data the assumed material behavior was elastic perfectly plastic and the predictions underestimated the measured stresses for all volume fractions. Nevertheless the model results were consistent with the experimental measurements. The transverse stress in the fibers is discussed in the context of the interface normal stress, which is significant to the global mechanical response.

# 1. INTRODUCTION

High temperature structural metal matrix composites (MMCs) typically consist of a compliant matrix with a creep resistant second phase in the form of particles, whiskers or fibers. High specific stiffness and strength make composites attractive for many applications, offering weight savings of between 25 and 50% compared to 'conventional' materials such as superalloys [1]. However, due to differences in the coefficient of thermal expansion of the constituents, residual stresses develop during processing. Their magnitude and distribution change with volume fraction and arrangement and affect fracture and interfacial behavior.

Tungsten fiber-reinforced Kanthal metal matrix is a model system developed (through collaboration between NASA's Lewis Research Center and Tufts University, Massachusetts), to explore performance in applications where high strength at high temperatures (1300 - 1700 K) is desired [1-6]. In particular the use of continuous fibers offers superior high temperature stability compared to discontinuous fiber composites.

The matrix alloy, Kanthal, belongs to a family of Fe-Cr-Al refractory alloys, which exhibit outstanding high-temperature oxidation resistance, mechanical behavior and weldability. Potential applications include corrosion resistant cladding or as a reactor fuel containment in space nuclear systems [5-9]. Other refractory metal alloys that are considered for high temperature structural applications are based on niobium and molybdenum [2-6].

To enhance Kanthal's strength tungsten fibers, which have a high melting temperature (3660 K [10]) and negligible creep below around 1273 K [11-13], are added. The disadvantage is the development of residual stress (due to the mismatch in the coefficient of thermal expansion between the Kanthal ($9.58 \times 10^{-6}$/K) and the tungsten ($4.4 \times 10^{-6}$/K)) during cooling from fabrication temperatures of around 1338 K. Since these residual stresses affect the composite creep and creep-rupture behavior [14-19], measurement and estimate of their magnitude is important. Ultimately they can cause cracking, interfacial debonding or yield of the matrix, degrading mechanical properties such as strength or fracture toughness [20,21]. Not all effects are detrimental, since friction at the fiber-matrix interface caused by residual stresses can, in some cases, improve the load transfer.

Considerable theoretical and modeling effort has been used to estimate the residual stress in particulate and fiber reinforced composites. Approaches range from elasticity theory applied to concentric cylinders [22-33] to finite element analyses of a unit cell surrounding a fiber [34-

51]. Conversely X-ray and neutron diffraction are commonly used for experimental assessment [52-57].

# 2.0 EXPERIMENTAL AND COMPUTATIONAL METHODS

## 2.1 Neutron Diffraction Measurements

Diffraction based stress analysis techniques utilize the distance between atomic planes of a crystalline specimen as an 'internal' strain gage [58]. When a crystalline material experiences a stress, elastic strains are manifested in a distortion of the crystal lattice. Applied or macro-residual stresses extending over many grains result in plane specific elastic strains that are measurable for different Bragg reflections.

Typical diffraction spectra (discussed later) are shown in **Fig. 1 (a,b)**. The spectra comprise peaks, which correspond to diffracting planes (characterized by their miller indices (hkl)) given by Bragg's law, $\lambda = 2\ d \sin(\theta)$ (where $\lambda$ is the wavelength of the incident spectra, d is the interplanar spacing, and $2\theta$ is the scattering angle for the peak). In the presence of a residual strain a diffracted peak will shift to higher or lower d spacing, according to whether it is tensile or compressive. The lattice plane normal for each peak lies parallel to the scattering vector (hereafter referred to as $\underline{Q}$) in the sample, and bisects the incident and diffracted beams. The strain $\varepsilon_{hkl}$ in this direction (parallel to the scattering vector) is given by,

$$\varepsilon_{hkl} = (d_{hkl} - d^0_{hkl}) / d^0_{hkl} \quad (1)$$

where $d^0_{hkl}$ is the plane spacing in the absence of a stress.

At a pulsed neutron source a diffraction pattern is recorded over a range of lattice spacings because the neutron beam consists of a range of wavelengths. The measurements in this study were performed using the neutron powder diffractometer (NPD) at the Manuel Lujan Jr. Neutron Scattering Center at Los Alamos National Laboratory using established methodology [34, 52,53].

Each sample was placed with the fiber axes horizontal and oriented at $45^o$ to the incident neutron beam. This allowed simultaneous measurement of lattice spacings parallel and perpendicular to the fiber axes, using opposing $90^o$ detector banks **(Fig. 2)**. Two other strain directions ($29^o$ and $61^o$ to the fiber axes) were recorded using the '$148^o$' detectors. Each detector bank comprises 31 individual $^3$He tubes that subtend a combined angle of about $11^o$ $2\theta$. Spectra

from individual tubes are integrated, with corrections for differences in diffraction angle and flight path, to provide a single spectrum for each detector bank.

The samples were mounted such that the neutron path length through their thickness was approximately 2.5mm irradiating a sampling volume of approximately 884 $mm^3$ in all cases. Diffraction spectra from the four banks were acquired simultaneously with a count time of ~2 hours per sample at a (proton) beam current of 70μA. Since the irradiated volume is appreciably larger than the comparable fiber volume, the strains are volume averaged. Strains measured at $0^o$ and $90^o$ to the fiber direction are referred to as longitudinal, $\varepsilon_L$, and transverse strains, $\varepsilon_T$, respectively.

**2.2 Models**

2.2.1 Modeling Introduction

Generally, where comparison between models and measurements are made either concentric cylinder (CC) or finite element model (FE) models are prevalent. Micro-mechanics models are used to predict local stress and strain variations around the fiber offering one approach to describe how the different microstructural phases affect the mechanical response.

2.2.2 Concentric Cylinder Model

One micro-mechanical model well suited (simple and easier to apply than finite element analysis) for investigating unidirectional composites is the concentric cylinder model [59]. Early versions, based on a single fiber embedded in a cylindrical shell [60-64] predicted elastic moduli or their bounds for general, three-dimensional loading, as well as thermoelastic and inelastic response under axisymmetric loading. Subsequent generalizations included the interaction of the composite cylinder with the surrounding (65-66), or accounted for microstructural details such as carbon coating around fibers, layered morphologies or interface layers (67-70) between the fiber and the matrix.

One model relevant to our geometry is the concentric cylinder assemblage (CCA) [71,72]. It was generalized to multi-layered configurations subject to axisymmetric thermomechanical loading, with layers exhibiting either elastic or elastoplastic behavior [73-74] (referred to as the multiple concentric cylinder model - MCCM). This generalization was facilitated by an analytical solution methodology based on the local-global stiffness matrix formulation of multi-layered boundary value problems [75-76], together with Mendelson's technique of successive iterations for elastoplastic problems [77]. Thus far, MCCM has been

successfully applied to the evolution of residual stresses in silicon carbide/titanium aluminide unidirectional composites, and to the subsequent axi-symmetric thermo-mechanical response [73,74]. Even though it neglects the interaction of the surrounding medium, its results are comparable to a modified self-consistent model where the surrounding medium is considered (65). The properties of the individual regions are allowed to vary with temperature, and both fiber and the surrounding, homogeneous matrix, exhibit inelastic effects.

The CC model used in this study comprised a series of 'infinitely' long multiple concentric cylinders or shells perfectly bonded to form the simple assembly shown in **Fig. 3**. Each shell is either elastic or inelastic. The elastic shells are isotropic, while the inelastic shells are initially isotropic but use time-independent incremental plasticity with isotropic hardening. The CCM represents a unit cell of a regular arrangement of fibers, consisting of a circular fiber of radius $r = r_f$ surrounded by a matrix sheath of radius $r = r_m$, measured from the fiber center, $r = 0$. The fiber volume fraction is proportional to the square of the ratio, $V_f = (r_f/r_m)^2$. Displacements and stresses in the individual phases are calculated under conditions of spatially uniform temperature changes. The elastoplastic boundary-value problem was solved using an assumption of generalized plane strain. The total strain formulation of the governing differential equations was employed within the framework of the so-called method of successive elastic solutions outlined by Mendelson [77]. When the stress distributions are elastic, they are characterized by uniform values of longitudinal stress throughout the fiber and the matrix and an inversely quadratic radial dependence of the hoop and radial stresses in the matrix.

By normalizing the radius of the composite cylinder to 1.0, the radii of the tungsten fibers were selected to be 0.316, 0.447, 0.548 and 0.837 to give fiber volume fractions of 10, 20, 30 and 70%. Furthermore, the fiber and matrix phases were divided into multiple cylinders to describe the plastic strain distributions. The number of layers depended on the volume fraction, but varied from a minimum of 10 to a maximum of 40. Plastic strains were calculated by evaluating integrals of the strain distribution at several points within each layer.

### 2.2.3 Finite Element Modeling

Although the study on this system is amenable to a CCM solution, many geometries are not and a FEM provides an alternative route to insights concerning the spatial distribution of stress and inelastic strains. In the past finite element models applied to composites have addressed; HIPing effects, fiber distribution and arrangement on residual stresses [40,44,48-51].

FE models can use either a full 3-D version, or, make 2-D plane field approximations, which include plane stress, plane strain, or generalized plane strain [37,46,47,78,79]. 2-D calculations are popular because of their reduced computational complexity and studies [37,46] For that reason we chose to use a generalized plane strain solution in which the entire composite contraction is considered allowing for a nonzero value for the out-of-plane strain component. FEM calculations were performed using a commercial finite-element code ABAQUS [80]. Unit cells with quarter symmetry and a square fiber array were modeled using 10-node bi-quadratic generalized plane strain elements (CGPE10). This represents a cross-section through a continuous infinitely long composite. Stress variations along the fiber and shear stresses on planes parallel to the fibers are assumed to be zero.

**Fig. 4** shows the mesh used for the 30 % $V_f$ model, with the fiber/matrix boundary emphasized. The left and bottom edges were constrained from moving in the horizontal and vertical directions, respectively. The top and right edges were constrained using multi-point constraints to remain horizontal and vertical, respectively, but allowed translation in a direction normal to the edge. The analysis used incremental plasticity, the Von Mises yield surface and the associated flow rule.

## 3.0 SPECIMENS

Tungsten/Kanthal composites containing 10, 20, 30, and 70 % $V_f$ GE 218 tungsten fibers (diameter ≈ 200 μm) were fabricated at NASA Lewis Research Center using the arc-spray method. The Kanthal matrix composition in weight % is; 73.2 Fe, 21 Cr, 5.8 Al, and 0.04 C [7]. Tapes containing unidirectional fibers were hot pressed at 1338K for 1 hour before being cooled to room temperature. The as-fabricated bars were approximately 25 mm wide, 2.5 mm thick, and 200 mm long. An additional monolithic Kanthal bar was fabricated and taken through the same heating cycle. All four composites exhibited fairly even distribution of fibers except for the 70% $V_f$ sample, which was densely packed and showed sporadic clustering [14,15], **(Fig. 5).**

## 4.0 EXPERIMENTAL RESULTS

### 4.1 Neutron Diffraction Single Peak Strains

The body centered cubic (BCC) tungsten fibers showed a strong <110> texture, therefore, only 2 independent hkl reflections (<n>110,211) are reported. By contrast, the Kanthal matrix (which is also BCC) exhibited close to random texture and four independent hkl reflections

(<n>110, <n>200, 222, 321) are reported. Only non-overlapping reflections with a height to background ratio of > 100:1 are reported. The diffraction patterns in **Fig. 1** illustrate the strength of the tungsten texture.

**Fig. 6 (a,b)** shows the measured d-spacings for the tungsten and Kanthal (110) reflections at different angles ($0^o$, $29^o$, $61^o$, and $90^o$) to the fiber direction. Using the measured d-spacings for the monolithic tungsten (100% $V_f$) and monolithic Kanthal (0% $V_f$), plane specific residual strains ($\varepsilon_{hkl}$) for a series of planes were calculated using equation 1. The angular dependence of the hkl strains for the 30% $V_f$ fiber composite are plotted in **Fig. 7**. The lines through the data correspond to fits of the form $\langle\varepsilon\rangle_{f,m} = \langle\varepsilon_{11}\rangle_{f,m}\cos^2\alpha + \langle\varepsilon_{22}\rangle_{f,m}\sin^2\alpha$, where f, m are the fiber and matrix, $\alpha$ is the angle to the fiber direction and $\varepsilon_{11}$ and $\varepsilon_{22}$ are the extremal strains.

In **Fig. 8a** the plane specific strains for (200), and (222) Kanthal reflections are plotted as a function of angle to the fiber orientation for the four different fiber volume fractions. The elastic anisotropic factor of Kanthal is close to that of pure iron 2.71. The (111) planes have the highest stiffness (*single crystal* elastic modulus ~ 273 GPa) and the (100) planes the least (*single crystal* elastic modulus ~ 125 GPa) [82]. The values in **Fig. 8a** reflect these differences, with the (200) and (222) planes representing the maximum and minimum strains, respectively. The trend is consistent for all four $V_f$.

In **Fig. 8b** the strains for the tungsten (110) and (211) reflections are plotted as a function of angle to the fiber orientation. Since the tungsten fibers exhibited a strong <110> texture the <n>(110) planes and (211) planes dominated the spectra with $\underline{Q}$ parallel to the fiber orientation (other planes were visible but were too weak to fit). By contrast with Kanthal, the elastic anisotropy factor for tungsten is 1.00 [81]. Accordingly, all the tungsten hkls have the same elastic moduli and, in the absence of plasticity, the strains are expected to be identical. This appears to be the case, except for the 10 vol. % fraction composite (which may be exhibiting plastic anisotropy associated with the large stresses and possible yield in the tungsten.

### 4.2 Neutron Diffraction Phase Average Strains using Rietveld Refinement

As seen above a range of the strains demonstrated by the Kanthal are hkl dependent due to the elastic and (presumably) to the plastic anisotropy of the polycrystal. To describe this spread with a single "macrostrain" for each phase the use of Rietveld refinement analysis is well suited for Time-of-Flight data [82-87]. In the Rietveld technique a spectrum is predicted and compared with measured data. The prediction is optimized to achieve the best agreement with

the measured spectrum by systematically varying microstructural parameters (lattice parameters, atomic positions and occupancies), peak shape parameters (strain and particle size), sample absorption, extinction, preferred orientation and Debye-Waller factors. Assuming that the lattice parameter is representative of the bulk, when a and $a_0$ are the phase specific lattice parameters of the composite and monolithic then the mean phase strains can be calculated using;

$$\varepsilon = (a - a_0) / a_0 \qquad (2)$$

Strains calculated from the lattice parameters are plotted in Fig. 9. The strains are maximum parallel ($0^o$) and minimum perpendicular ($90^o$) to the fibers for all four $V_f$ in both Kanthal and tungsten. Parallel to the fibers the strains in the Kanthal are tensile and increase from + 300 με to + 3300 με as $V_f$ increases from 10 to 70%. Conversely, the longitudinal strains in the tungsten are compressive and decrease from -3500 με to -700 με as the $V_f$ increases from 10 to 70%. The transverse strains in the Kanthal are compressive for $V_f$ = 10 and 20 vol. %, decreasing from -251 με to -53 με. However, for $V_f$ = 30 and 70 vol. %, the Kanthal transverse strains are tensile, with values of 78 and 814 με. The transverse strains in the fibers are, in all cases, compressive and decrease from -135 to -78 με. Typical error bars on these strain values are ± 100 με.

# 5.0 MODEL - RESULTS

## 5.1 Model Assumption

In the models (section 2.2 & 2.3) we assumed that the difference between the thermal expansion coefficients of the components constitutes the only source of residual stress. Non-uniform cooling or phase transformations were not considered. Because creep properties were not available viscoelastic/viscoplastic behavior was not considered and, instead we assumed a stress-free (or freezing) temperature of 923K (the processing temperature was 1338K). The value of 923K was taken from a previously reported result [14,15]. It is also consistent with the work of Kroupa et al [88] who showed, using the Bodner-Partom model that a bilinear elastic-plastic FEM analysis could predict comparable residual stresses (in a titanium matrix composite) to a viscoelastic/viscoplastic analysis provided that the stress-free temperature was ≈ 0.7 - 0.8 times of the absolute processing temperature. In the absence of any strain hardening data, bilinear thermo-elastic-perfectly plastic analysis was assumed. Equivalent material properties were used in both models and are reported in **Tables 1 and 2**.

### 5.2 Model Strains

Spatial elastic strain distributions predicted using the concentric cylinder model for the longitudinal, radial and hoop components, are shown for 10, 20, 30 and 70 % $V_f$ composite **(Fig. 10 a-c)**. In the tungsten all three strains (longitudinal, radial and hoop) are constant at all radii. In the Kanthal, the longitudinal strain is comparatively uniform across the radius, whereas the radial and hoop distributions adopt an inversely quadratic dependence away from the region close to the interface. Residual strains contours are plotted for the 30 % $V_f$ FEM calculation in **Fig. 11**. Contour maps for the 10,20 and 70 % $V_f$ composites are qualitatively similar but differ in magnitude.

### 5.3 Strains - ND, CCM and FEM

Since the neutron measurements irradiate the entire cross-section of the composite the measured elastic lattice strains are necessarily a volume average (see **Fig. 2**). Thus for comparison with the models it was necessary to convolute the models with a resolution function that is descriptive of the experiment. In the longitudinal direction, where the strain shows little radial variation it is straightforward to obtain an integrated result averaged over the composite cross-section. However, for the transverse direction, the neutron measurement does not distinguish between radial and hoop, and comparison with the models requires that this is accounted for. For the tungsten the radial and hoop strains are at least constant across the radius albeit of different sign (**Fig. 10 b-c**). However, for the Kanthal, the radial and hoop strains vary in space, magnitude and sign. To express the model results as an average transverse strain where, $\langle\varepsilon\rangle_r$ and $\langle\varepsilon\rangle_h$ are the integrated average strains for the radial and hoop components (see **Appendix A**) we used;

$$\langle\varepsilon\rangle_T = 2/\pi\ (\langle\varepsilon\rangle_r + \langle\varepsilon\rangle_h) \qquad (3)$$

The coefficients of thermal expansion for the Kanthal ($\alpha_m = 9.58 \times 10^{-6}$/K) and tungsten ($\alpha_f = 4.4 \times 10^{-6}$/K), dictate that the longitudinal strains for the matrix and fiber are expected to be tensile and compressive respectively. The FE values are consistently about 20% larger than the CC values but for the 10,20,30 % samples both are comparable to the neutron results within experimental error (**Table 3**). However, for the 70 % $V_f$ , the predictions significantly underestimate the ND value. Similar observations can be made for the tungsten.

The average transverse strains (**Table 4**) are relatively small due to the offsetting signs of the radial and hoop strains. Indeed for some $V_f$ the average transverse strain is more than an

order of magnitude less than the longitudinal strains. Although there are trends in the transverse direction the patterns of behavior are harder to discern and are not intuitive. However it is noted that whereas the CC and FE values track one another in sense (if not in magnitude) the model predictions fail to describe the experimental results.

### 5.4 Stresses - ND, CCM and FEM

Stresses were calculated using Hooke's law (subject to the assumption of isotropy) using the elastic strains reported in Tables 3 and 4 and room temperature material properties from tables 1 and 2.

$$\sigma_L = \frac{E}{(1+\nu)(1-2\nu)}((1-\nu)\varepsilon_L + 2\nu\varepsilon_T) \quad (4)$$

$$\sigma_T = \frac{E}{(1+\nu)(1-2\nu)}(\nu\varepsilon_L + \varepsilon_T) \quad (5)$$

Longitudinal, $\sigma_L$ and transverse, $\sigma_T$ residual stresses are plotted for ND, CCM and FEM in **Figs. 12 and 13,** respectively. In **Fig. 12**, with increase in $V_f$ from 10 to 70% the ND measured longitudinal stresses in the Kanthal increase from approximately 40 MPa (10% $V_f$) to 1100 MPa (70 % $V_f$) whereas the compressive stress in the fiber decrease from approximately -1877 MPa (10% $V_f$) to -400 MPa (70% $V_f$). The CC and FE predictions track the behavior but underestimate the magnitudes and (for the Kanthal) show disparities at the 10 and 70 % $V_f$.

In **Fig. 13**, the ND measured transverse stress in the Kanthal varies from (-56 MPa) for the 10% $V_f$ to a tensile value of 729 MPa for the 70% $V_f$. Correspondingly, the compressive stresses in tungsten vary from -880 to -218 MPa as $V_f$ increases from 10 to 70%. The CCM predictions for the Kanthal increase from 66 MPa to 273 MPa complemented by tungsten stresses decreasing from –573 MPa to -116 MPa with $V_f$. The FEM predictions, predict tensile stresses in the Kanthal increasing from 54 MPa to 270 MPa and decreasing stresses in the tungsten from –494 MPa to -113 MPa with increase in $V_f$.

For context using a thermo-*elastic* analysis we considered the upper and lower bounds of the longitudinal stress in the matrix of a concentric cylinder based on a thermo-elasticity solution. An upper limit, independent of volume fraction, is provided when considering a thin matrix surrounding a rigid fiber for which the longitudinal Kanthal stress is $(\alpha_m-\alpha_f)E_m/(1-\nu_m)$ = 959 MPa. Not surprisingly this is higher than 70 % $V_f$ CCM value of 501 MPa but is still lower than measured value of 1111 MPa. For a lower limit one might assume free thermal contraction

in the transverse direction and assumes the elastic fiber constrains the matrix axially. In this case, the longitudinal Kanthal stresses is given by $(\alpha_m-\alpha_f)E_mE_fV_f/(E_mV_m + E_fV_f)$ from which for the 70% $V_f$ the stress is 855 MPa, respectively. In the absence of plasticity these limits are, not surprisingly, higher than those predicted by the CCM model but are also both less than the measured value which must be addressed. The small differences between the FEM and CCM results can be ascribed to differences in constraint and boundary conditions between the models.

# 6.0 DISCUSSION

## 6.1 Stress comparison (ND, CCM and FEM)

In figures 12 and 13 the experimental and modeled stresses show encouraging agreement both in trend and in value. Although the models underestimate the experimentally measured stress the difference can, likely, be ascribed to the absence of hardening in the material descriptions. This is also consistent with the measured longitudinal stresses in the Kanthal which exceeded the "nominal" room temperature yield stresses (used in the models) by more than 50% in the 70% volume fraction sample. Further supporting evidence comes from the FE predictions which indicated that plasticity occurred in the Kanthal for all 4 tungsten volume fractions and had initiated in the tungsten for the 10 % $V_f$ (Fig 14). In view of the absence of creep data in the model we opted not to "tune" the stress free temperature for better agreement but note that the assumption of 0.7 – 0.8 of the processing temperature appears plausible. (As an aside we note that our FEM predicted stresses are higher than those previously reported by Saigal and Leisk because we corrected a small error concerning the thermal expansion coefficients in their calculations [14-15]).

Apart from the trendswhich are reasonable, two major points of experiment-model disparity occur for the Kanthal longitudinal stress for the 10 and 70 % $V_f$ results. For the larger tungsten volume fraction the stress and plasticity in the Kanthal is largest, thus this sample would be expected to show the biggest disparity from an assumption of elastic *perfectly plastic* behavior. Moreover the relationship between work hardening and volume fraction is more likely to contribute for larger volume fractions [89,90-93]. One reason being the impediment of dislocation movement by the elastic fiber response when the matrix deforms plastically. This impeding or matrix strengthening stress is proportional to the fiber volume fraction, $V_f$, and the accumulated plastic strain, $e_{p,}$ according to $s_{M,m} = 2Ke_pG_fG_mV_f / G_f - K(G_f-G_m)$, where $K$ is an accommodation factor between fiber and matrix and $e_p$ is the accumulated plastic strain.

For the 10 % $V_f$ sample the disparity is harder to explain. We tested the viability of the neutron measurements by checking whether they obeyed stress balance using the relation, $s_f V_f + s_m V_m = 0$. As shown in Figure 12 the stress balance is satisfied to within experimental error for the 20, 30 and 70 % $V_f$ but not for the 10 % $V_f$ . Accordingly the disparity between measurement and experiment for the 10 % $V_f$ may be due to experimental error.

### 6.2 Localized and volume averaged behavior

The longitudinal strains (which are measured uniquely in the experiment) are reasonably uniform across the sampling volume (Figs 10 and 11) and thus are amenable to volume averaging for direct comparison with the neutron results. However the inability of neutron measurements to directly measure localized behavior is a practical impediment, which leads to some inelegant averaging schemes to compare the model and experiment. Averages of the radial and hoop strains to compare with the measured transverse response involve values that vary in sign and magnitude with respect to one another and across the sampling volume. This makes the averaging scheme prone to systematic errors and insensitive to changes in deformation path. Indeed the disparities in the average transverse behavior reported in table 4 for the experiment and (both) models merits future attention.

Despite the limitation of these measurements to address localized effects one reason for considering length scales comparable to the fiber diameter is the expected range of dislocation density and associated potential for changes in the microstructure near the fiber matrix interface. A few researchers have shown using transmission electron microscopy and electron back scattering patterns from scanning electron microscopy that the matrix characteristics close to the interface differ from those of the monolithic material [94-97]. It is speculated that increasing dislocation density causes the stored energy to reach a threshold upon which the only way of relieving this energy is by rearranging the microstructure with a finer grain size. Since this can produce differences in mechanical performance it has the potential to create an interface zone that is not described in either the FE or CC models. Characterizing the thin interface zone is within the realms of current synchrotron XRD measurements but is beyond the scope of this study.

### 6.3 Radial Interface Stresses

Transverse and longitudinal properties of continuous fiber reinforced composites are influenced by the properties of the fiber/matrix interface. For example in a study of interface

creep in a fiber reinforced metal-matrix composite [98] it was shown that threshold deformation behavior for sliding between fiber and matrix, during a fiber push-down test at elevated temperatures, was directly related to the normal (radial) residual stress acting on the interface. Accordingly measurement of the bond strength must account for the presence of any transverse residual stress, which must be overcome before interface separation can occur. Interface bond strength is expressed by;

$$\sigma_{bond} = \beta K \sigma_{applied} + \sigma_{residual} \qquad (6)$$

Where K (≈ 1.2-1.3) is the stress concentration factor at the interface debond site due to the elastic modulus mismatch effect, $\beta$ is a multiplication factor, which ranges from unity (no sliding) to 1.34 (freely sliding interface). $\sigma_{applied}$ is the far-field applied stress required to cause debonding (normal interface separation) and $\sigma_{residual}$ is the radial (transverse) residual stress at the debond site [50]. Note that for a compressive normal stress $\sigma_{residual}$ is negative.

Some researchers have used volume averaged neutron data to estimate the value of the radial stress local to the interface [33]. Such estimates are based on predictions of the concentric cylinder model. Because the concentric cylinder model predicts that radial and hoop stresses are (1) equal to each other and (2) uniform in the fiber (Figure 10), the radial interface stress would be equal to the average transverse stress in the fiber. Hence, transverse fiber stresses measured by neutron diffraction could be used as an estimate of the radial interface stress (Figure 13). However, the finite element simulations in this paper indicate that such a conclusion is only valid for relatively small fiber volume fractions (e.g,. up to 20% in the specimens studies here). For larger volume fractions, neighboring fibers destroy the axisymmetry assumed by the CCM, and the interface radial stress differs significantly from the average transverse stresses in the fiber. It is worth noting that techniques such as nanoindentation; microindentation; acoustic emission; extended X-ray absorption fine structure (EXAFS) have all been used to estimate radial stresses at the fiber/matrix interface. However, the results of these techniques are often difficult to interpret.

## 7. CONCLUSIONS

Mean phase elastic strains and stresses are reported in Kanthal matrix composite samples reinforced with four volume fractions of unidirectional tungsten fibers. Maximum and minimum longitudinal stresses were –1900 and –400 MPa for the tungsten for 10 and 70% respectively.

For the Kanthal maximum and minimum longitudinal stresses were 1100 and 40 MPa for the 70 and 10% samples respectively. Stress balance parallel to the fiber direction were within experimental error for the 20,30 and 70% samples but exceeded experimental error for the results from the 10% sample. Comparisons with finite element and concentric cylinder models were qualitatively adequate but, in the absence of either hardening description for the room temperature mechanical behavior or of viscoelastic description for the high temperature behavior, quantitative predictions were not possible. It is suggested that the radial stress at the matrix/fiber interface can be inferred from the transverse fiber stress, which is likely to be uniform across the cross section.

## 8. ACKNOWLEDGMENTS

This work was supported (in part) under the auspices of the United States Department of Energy. The Lujan Scattering Center is a national user facility funded by the United States Department of Energy, Office of Basic Energy Sciences - Materials Science, under contract number W-7405-ENG-36 with the University of California. IJB is grateful for the support provided by a J. R. Oppenheimer Fellowship.

## 9. APPENDIX

The derivation of the average transverse strain component from the discrete radial and hoop strains is given in the following way. The volume element in a cylindrical coordinate system is shown in Figure A1.

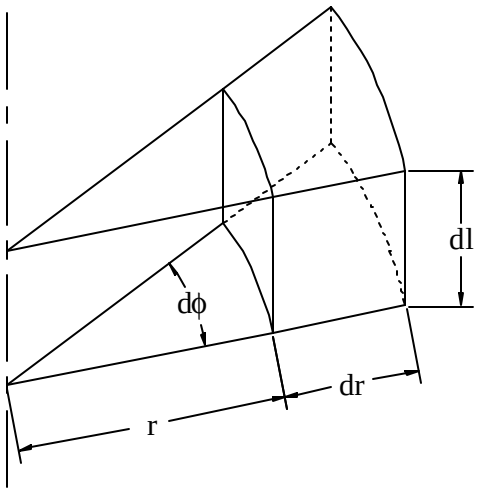


**Figure A1:** Volume element in cylindrical coordinate system.

The average transverse strain (the strain in the direction of a scattering vector perpendicular to the longitudinal axis of a cylindrical sample) is found as

$$\bar{e} = \frac{4\int_0^L\int_0^R\int_0^{p/2}(e_r\cos f + e_h\sin f)\,r\,df\,dr\,dl}{4\int_0^L\int_0^R\int_0^{p/2} r\,df\,dr\,dl} \tag{A1}$$

where $L$ and $R$ are the length and radius of the sample, respectively. The denominator is the total volume. The total volume of the FE model is also given by the sum of all the element volumes, and we find that

$$4\int_0^L\int_0^R\int_0^{p/2} r\,df\,dr\,dl \;= \text{Total volume} = \sum_{i=1}^{N} volE^i \tag{A2}$$

where $volE^i$ is the volume of element $i$ in the FE mesh. By reducing equation (B1), the average transverse strain can be found as

$$\bar{e} = \frac{2p\int_0^L\int_0^R \frac{2}{p}(e_r + e_h)\,r\,dr\,dl}{2p\int_0^L\int_0^R r\,dr\,dl} \tag{A3}$$

And thereby, the average transverse strain in terms of the finite element calculations can be found as

$$\bar{e} = \frac{\sum_{i=1}^{N}\frac{2}{p}(e_r^i + e_h^i)volE^i}{\sum_{i=1}^{N} volE^i} = \frac{\frac{2}{p}\left[\sum_{i=1}^{N} e_r^i volE^i + \sum_{i=1}^{N} e_h^i volE^i\right]}{\sum_{i=1}^{N} volE^i} \tag{A4}$$

since the radial and hoop strains are independent variables. If we define the average radial and hoop strains as

$$\bar{e}_r = \frac{\sum_{i=1}^{N} e_r^i volE^i}{\sum_{i=1}^{N} volE^i} \quad \text{and} \quad \bar{e}_h = \frac{\sum_{i=1}^{N} e_h^i volE^i}{\sum_{i=1}^{N} volE^i} \tag{A5}$$

the overall average transverse strain is found as

$$\bar{e} = \frac{2}{p}\left(\bar{e}_r + \bar{e}_h\right) \tag{A6}$$

# 10. REFERENCES


1. J. E. Schoutens, Journal of Metals, Page 43, June 1985.
2. J. Wittenauer, Journal of Metals, Page 7, August 1990.
3. D. W. Petrasek, D.L. McDanels, L. J. Westfall and J. R. Stephens, Metal Progress, Page 27-31, August 1986.
4. R. H. Tritan, T. L. Grobstein, Journal of Metals, Page 8-10, August 1990.
5. R. A. Signorelli and J. A. Dicarlo, Journal of Metals, Page 41-42, June 1985.
6. R.H. Titran, J. R. Stephens, D. W. Petrasek, Journal of Metals, v. 40(#77) pp. A63-63, 1988.

7. C.T. Liu, V.K. Sikka and C.G. McKamey, 1993, Alloy Development of FeAl Alloys for Structural Use in Corrosive Environments, Oak Ridge National Laboratory, ORNL/TM-12199.
8. J.E. Antill and K.A. Peakall, J. Iron Steel Inst., 205, pp. 1136, 1967.
9. P. J. Maziasz, G.M. Goodwin, C. T. Liu and S. A. David, 1992, Scripta Metall. Mat., 27, pp. 1835.
10. A. Kelly, Strong Solids, Clarendon Press, Oxford, p. 115, 1966.
11. T. W. Clyne and P. J. Withers, An introduction to metal matrix composites, Cambridge University Press, New York, p. 480, 1993.
12. W. V. Green, Transactions of the Metallurgical Society of AIME, Vol. 215, pp 1057-1060, Dec. 1959.
13. W. D. Klopp, W. R. Witzke and P. L. Raffo, Transactions of the Metallurgical Society of AIME, Vol. 233, pp. 1860-1866, Oct. 1965.
14. A. Saigal, G.G. Leisk, S.T. Misture, C.R. Hubbard, 1996, Scripta Materialia, v. 34, (#8), pp. 1309,1319.
15. A. Saigal, G. C. Leisk, Materials Science and Engineering, A237, pp. 65-71 (1997).
16. P. Rangaswamy, M. A. M. Bourke, A. Saigal, "Effect of Reinforcement Volume Fraction on Residual Strain and Stress in Fiber-Reinforced Tungsten/Kanthal Metal Matrix Composites", FATIGUE, FRACTURE, AND RESIDUAL STRESSES, PVP-Vol. 373, Pages 267-279. Presented at THE 1998 ASME/JSME JOINT PRESSURE VESSELS AND PIPING CONFERENCE, San Diego, California, July 26-30, 1998.
17. W.K. Binienda, D.N. Robinson, S.M. Arnold and P. A. Bartolotta, A Creep Model for Metallic Composition Based on Matrix Testing: Application to Kanthal Composites, NASA TM 103172, 1990.
18. W.K. Binienda and D. N. Robinson, Journal of Engineering Mechanics, Vol. 117, No. 3, pp. 624-639, Mar. 1991.
19. D. N. Robinson, W.K. Binienda and M. Miti-Kavuma, Journal of Engineering Mechanics, Vol. 228, No. 8, pp. 1646-1660, Aug. 1992.
20. M. Taya and R. J. Arsenault, "Metal Matrix Composites - Thermomechanical Behavior," pp. 103-104, 1989.
21. S. Mukherjee, C. R. Ananth, and N. Chandra, Effect of residual stresses on the interfacial fracture behavior of metal-matrix composites, Composites Science and Technology, 57 , 1501-1512, 1997.
22. S. S. Hecker, C. H. Hamilton and L. J. Ebert, Journal of Materials, JMLSA, Vol. 5, No. 4, pp. 868-900, Dec. 1970.
23. R. J. Arsenault and M. Taya, Acta metall., Vol. 35, No. 3, pp. 651-659, 1987.
24. M. J. Pindera, A. D. Freed, Journal of Engineering Materials and Technology-Transactions of the ASME , v. 116(#2) pp. 215-221, Apr. 1994
25. M. J. Pindera, R. S. Salazar and T. O. Williams, Composites Engineering, v. 3(#12) pp. 1185-1201, 1993.
26. M. J. Pindera and T. O. Williams, Composites Engineering, Vol. 4, No. 1, pp. 129-145, 1994.
27. T. O. Williams, S. M. Arnold, M. J. Pindera, "Effectiveness of Graded Interfacial Layers in Reducing Residual Stresses in Titanium Matrix Composites", Residual Stresses in Composites: Measurement, Modeling and Effect on Thermo-Mechanical Properties, E.V. Barrera, I. Dutta, and S.G. Fishman, Eds., A publication of The Minerals, Metals & Materials Society (TMS), pp 187-206 , Feb 21-25, 1993.
28. M. Uemura, H. Iyama, and Y. Yamaguchi, Residual stresses in filament-wound-carbon-fiber-reinforced composites, Journal of Thermal Stresses, **2**, pp. 393-412, 1979.
29. J. A. Nairn, Thermoelastic analysis of residual stresses in unidirectional, high-performance composites. Polymer Composites, **6**, 123-130, 1985.
30. M. Vedula, R. N. Pangborn, R. A. Queeney, COMPOSITES , v. 19(#1) pp. 55-60, 1988.
31. M. Vedula, R. N. Pangborn, R. A. Queeney, COMPOSITES , v. 19(#2) pp. 133-137, 1988.
32. H. Zhang, P. M. Anderson and G. S. Daehn, Metallurgical and Materials Transactions (A), Vol. 25A, pp 415-425, Feb. 1994.
33. P.K. Wright, M. D. Sensmeier and M. Lococo, "Thermal Stress Effects in Intermetallic Matrix Composites," Residual Stresses in Composites: Measurement, Modeling and Effect on Thermo-Mechanical Properties, E.V. Barrera, I. Dutta, and S.G. Fishman, Eds., A publication of The Minerals, Metals & Materials Society (TMS), Pp 207-218, Feb 21-25, 1993.
34. P. Rangaswamy, M.A.M. Bourke, P.K. Wright, E. Kartzmark, J.A. Roberts and N. Jayaraman, Materials Science & Engineering A224, pp. 200-209, 1997.
35. C.A. Bigelow, W.S. Johnson and A.R. Naik, Mechanics of Composite Materials and Structures, J.N. Reddy and J.L. Telpy, Eds., 1989.
36. A. Saigal, D.S. Kupperman and S. Majumdar, Materials Science and Engineering, AI50, pp. 59-66, 1992.

37. N. Chandra, C. R. Ananth and H. Garmestani, Journal of Composites Technology and Research, JCTRER, Vol. 16, No. 1, pp. 37-46, January 1994.
38. J.L.Kroupa : "Elastic-Plastic FEM analysis of MMC subjected to Thermomechanical Fatigue", in Proceedings from Titanium Aluminide Composite Workshop, eds. P.R. Smith, S.J. Balsone and T. Nicholas, WL-TR-91-4020, Materials Behavior Branch, Wright Laboratory, WPAFP (1991).
39. R. P. Nimmer, P.A. Siemers, M.R. Eggleston and E.S. Russel: Journal of Composites Technology & Research, Vol. 12, No. 2, pp. 65-75, 1990.
40. B. F. Sorensen and R. Talreja, Mechanics of Materials 16, pp-351-363, 1993.
41. P. Rangaswamy, W.C. Revelos and N. Jayaraman, Journal of Composites and Technology Research, (JCTRER), Vol. 16, No. 1, pp. 54-67, Jan. 1994.
42. L. J. Ghosn and S. V. Raj, "Modeling the Mechanical Response of a Nb-1Zr/218W Composite System", Modeling the Mechanical Response of Structural Materials, E. M. Taleff and R. K. Mahidhara, Eds., A publication of The Minerals, Metals & Materials Society (TMS), pp 45-52, 1997.
43. A. J. Wilkinson, Scripta Metallurgica et Materialia, Vol. 26, pp. 387-392, 1992.
44. J. F. Durodola and B. Derby, Acta metall. mater. Vol. 42, No. 5, pp. 1525-1534, 1994.
45. M. R. Wisnon, Journal of Composite Materials, Vol. 24, pp 707-725, July 1990.
46. R. P. Nimmer, Journal of Composites Technology & Research, JCTRER, Vol. 12, No. 2, pp. 65-75, Summer 1990.
47. R. P. Nimmer, R. J. Bankert, E. S. Russell, G. A. Smith and P. K. Wright, Journal of Composites Technology & Research, JCTRER, Vol. 13, No. 1, pp. 3-13, Spring 1991.
48. C. A. Bigelow, Journal of Composites Technology and Research, JCTRER, Vol. 14, No. 4, pp. 211-220, Winter 1992.
49. R. P. Nimmer, P. A. Siemers and M. R. Eggleston, Composites Engineering, Vol. 4, No. 12, pp. 1289-1305, 1994.
50. S. G. Warrier, P. Rangaswamy, M. A. M. Bourke and S. Krishnamurthy, Materials Science and Engineering, A259, pp 220-227, 1999.
51. J. R. Brockenbrough, S. Suresh and H. A. Wienecke, Acta Metall. Mater. Vol. 39, No. 5, pp. 735-752, 1991.
52. M.R. James, M.A. Bourke, J.A. Goldstone and A.C. Lawson, "Residual Stress Measurements in Continuous Fiber Titanium Matrix Composites," Advances in X-ray Analysis, Vol. 36, 1993.
53. M.R. James, "Residual Stresses in Metal Matrix Composites," International Conference on Residual Stresses II, G. Beck, S. Denis, and A. Simon, Eds., Elsevier, pp. 429-35, 1989.
54. P. Rangaswamy, W.C. Revelos and N. Jayaraman, Journal of Composites and Technology Research, (JCTRER), Vol. 16, No. 1, pp. 47-53, 1994.
55. P. Rangaswamy, and N. Jayaraman, Journal of Composites and Technology Research, (JCTRER), Vol. 17, No. 1, pp. 43-49, January 1995.
56. B.N. Cox, M.R. James, D.B. Marshall, and R.C. Addison, Jr., Metallurgical Transactions A, Vol. 21 A, pp. 2701, 1990.
57. H.F. Poulsen, T. Lorentzen, R. Feidenhansl, Y. L. Liu,Metallurgical and Materials Transactions A-Physical Metallurgy And Materials Science, v. 28(#1) pp. 237-243 Jan. 1997.
58. I.C. Noyan and J. B. Cohen, Residual Stress (New York, Springer Verlag, 1987).
59. J. Aboudi, "Mechanics of Composite Materials - A Unified Micromechanical Approach", Elsevier, New York, 1991.
60. Z. Hashin, J. Applied Mechanics, 29, 143-150, 1962.
61. R. Hill, J. Mechanics of Physics of Solids, 12, 213-218, 1965.
62. J. F. Mulhern, T. G. Rogers, A.J.M. Spencer, J. Inst. Maths. Applications 3, 21-40, 1967.
63. G. J. Dvorak and M.S.M. Rao, J. Applied. Mechanic, 98, 619-624, 1976a.
64. G. J. Dvorak and M.S.M. Rao, J. Applied. Mechanic, 98, 619-624, 1976b.
65. G. J. Dvorak and Y. A. Bahei-El-Din, J. Mech. Phys. Solid, 27, 51-72, 1979.
66. R.M. Christensen and K.H. Lo, J. Mech. Phys. Solids, 27(4), 51-72, 1979.
67. Z. Hashin, Mech. Materials, 8, 293-308, 1990.
68. Y. Benvensite, G. J. Dvorak and T. Chen, 12, 289-297, 1991.
69. M. Sutcu, Int. J. Solids Structures 29, 197-213, 1992.
70. C. W. Warwick and T. W. Clyne, J. Materials Science, 26, 3817-3827, 1991.
71. Z. Hashin and B. W. Rosen, J. Applied Mechanics, pp 223-232, 1964.
72. Z. Hashin, "Theory of Fiber Reinforced Materials", NASA CR-1974, Langley Research Center, VA, 1972.

73. M. J. Pindera, A. D. Freed and S. M. Arnold, International Journal of Solids & Structures, 30(9), 1213, 1993.
74. M. J. Pindera, R. S. Salazar and T. O. Williams, Composites Engineering 4(1), 129, 1993.
75. H. Bufler, Journal of Elasticity, 1, 125, 1971.
76. M. J. Pindera, Composites Engineering, 1(2), 69, 1991.
77. A. Mendelson, Plasticity: Theory and Applications, Robert E. Krieger Publishing Company, Malabar, Florida, 1983.
78. S. M. Arnold, V. K. Arya and M. E. Melis, "Elastic/Plastic Analyses of Advanced Composites Investigating the Use of the Compliant Layer Concept in Reducing Reduces Resulting from Processing", NASA TM 103204, 1990.
79. A. L. Highsmith, D. Shin and R. A. Naik, "Local Stresses in Metal Matrix Composites Subjected to Thermal and Mechanical Loading", Thermal and Mechanical Behavior of Metal Matrix and Ceramic Matrix Composites, ASTM STP 1080, J. M. Kennedy, H. H. Moeller, and W. S. Johnson, Eds., American Society for Testing and Materials, Philadelphia, pp. 3-19, 1990.
80. HKS Inc.: ABAQUS User's Manual, Providence, RI, USA, (1999).
81. R. W. Hertzberg, Deformation and Fracture Mechanics of Engineering Materials, Wiley, New York, p. 13f., 1976.
82. M. R. Daymond, M. A. M. Bourke, R. B. Von Dreele, B. Clausen and T. Lorentzen, Journal Applied Physics 82 (4), 1997.
83. H. M. Rietveld, Journal of Applied Crystallography, 2, pp 65 (1969).
84. A. C. Lawson and R. B. Von Dreele, Generalized Crystal Structural Analysis System (GSAS), Los Alamos National Laboratory, LAUR 86-748, (1966).
85. R. B. Von Dreele, J. D. Jorgensen, & C. G. Windsor, Journal of Applied Crystallography 15, 581, (1982).
86. L. B. McCusker, R. B. Vondreele, D. E. Cox, D. Louer and P. Scardi, Journal of Applied Crystallography, 32, pp 36-50, 1999.
87. R. B. Vondreele, Journal of Applied Crystallography, 30, pp. 517-525, 1998.
88. J.L. Kroupa and R.W. Neu, Composite Engineering, vol. 4, pp. 965-977. 1994.
89. S. M. Pickard and D. B. Miracle, Materials Science and Engineering, A203, pp. 59-68 (1995).
90. L. M. Brown and D. R. Clarke, Acta Metallurgica Vol. 25, pp. 563-570, 1977.
91. L. M. Brown and D. R. Clarke, Acta Metallurgica, Vol. 23, pp. 821-830, 1975.
92. R. J. Arsenault and N. Shi, Materials Science and Engineering, 81, pp 175-187, 1986.
93. P. J. Maziasz, G. M. Goodwin, C. T. Liu and S. A. David, Scripta Metallurgica et Materialia, Vol. 27, pp. 1835-1840, 1992.
94. A. J. Wilkinson and D. J. Dingley, Acta metall. mater., Vol. 40, No. 12, pp. 3357-3368, 1992.
95. A. J. Wilkinson and D. J. Dingley, Materials Science and Engineering, A135, pp. 189-193, (1991).
96. A. J. Wilkinson, "Probing local strain fields using electron diffraction in the scanning electron microscope", Inst. Physt. Conf. Ser. No. 153: Section 7, Paper presented at Electron Microscopy and Analysis Group Conf. EMAG97, IOP Publishing Ltd., Cambridge, pp. 221-227, 1997.
97. H. M. Yun and R. H. Titran, Metallurgical Transactions, Volume 23A, 3121-3133, Nov. 1992.
98. J. V. Funn, I. Dutta, Acta Materialia , V. 47(#1) Pp. 149-164 Dec 11, 1998.

# 11. LIST OF TABLES

## 12. LIST OF FIGURES

**Table 1: Tungsten: thermo-mechanical properties used in the models.**

| Temp. $^{o}$C | Young's Modulus (GPa) | Poisson's Ratio | Yield Stress (MPa) | Coefficient of Thermal Expansion ($10^{-6}/^{o}$K) |
|---|---|---|---|---|
| 26 | 395 | .28 | 1305 | 4.40 |
| 138 | 394 | .28 | 1179 | 4.42 |
| 251 | 393 | .28 | 1054 | 4.44 |
| 420 | 389 | .28 | 893 | 4.47 |
| 533 | 386 | .28 | 777 | 4.49 |
| 1000 | 360 | .28 | 550 | 4.56 |

**Table 2: Kanthal: thermo-mechanical properties used in the models.**

| Temp. $^{o}$C | Young's Modulus (GPa) | Poisson's Ratio | Yield Stress (MPa) | Coefficient of Thermal Expansion ($10^{-6}/^{o}$K) |
|---|---|---|---|---|
| 26 | 202 | .28 | 530 | 9.58 |
| 138 | 196 | .28 | 520 | 9.68 |
| 251 | 183 | .28 | 465 | 10.08 |
| 420 | 172 | .28 | 375 | 10.80 |
| 533 | 162 | .28 | 275 | 11.38 |
| 1000 | 125 | .28 | 27 | 14.75 |

**Table 3: ND, CCM and FEM Average Longitudinal Strains (με)**

Kanthal

| Tungsten Volume Fraction | ND Elastic | CCM Elastic | FEM Elastic | FEM *Plastic* |
|---|---|---|---|---|
| 10 % | 375 (± 279) | 688 | 833 | 67 |
| 20 % | 1397 (± 159) | 1242 | 1487 | 278 |
| 30 % | 1889 (± 140) | 1652 | 1884 | 677 |
| 70 % | 3263 (± 071) | 1902 | 2386 | 1881 |

Tungsten

| Tungsten Volume Fraction | ND Elastic | CCM Elastic | FEM Elastic | FEM *Plastic* |
|---|---|---|---|---|
| 10 % | -3459 (± 276) | -3151 | -3847 | -69 |
| 20 % | -2890 (± 232) | -2524 | -3050 | 0 |
| 30 % | -2367 (± 161) | -1945 | -2255 | 0 |
| 70 % | -710 (± 117) | -414 | -548 | 0 |

**Table 4: ND, CCM and FEM Average Transverse Strains (με)**

Kanthal

| Tungsten Volume Fraction | ND Elastic | CCM Elastic | FEM Elastic | FEM *Plastic* |
|---|---|---|---|---|
| 10 % | -251 (±212) | -62 | -83 | -33 |
| 20 % | -53 (±107) | -100 | -150 | -139 |
| 30 % | 78 (±122) | -114 | -200 | -338 |
| 70 % | 814 (±153) | 82 | 84 | -941 |

Tungsten

| Tungsten Volume Fraction | ND Elastic | CCM Elastic | FEM Elastic | FEM *Plastic* |
|---|---|---|---|---|
| 10 % | -135 (±178) | 306 | 392 | 35 |
| 20 % | -59 (±89) | 214 | 317 | 0 |
| 30 % | -87 (±121) | 140 | 244 | 0 |
| 70 % | -78 (±67) | -18 | -5 | 0 |

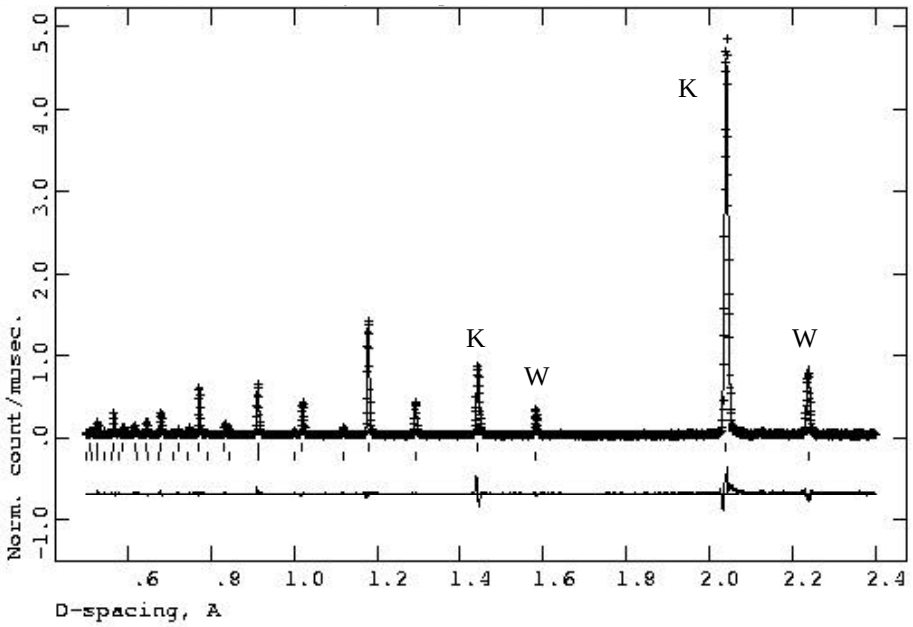


**(a)**

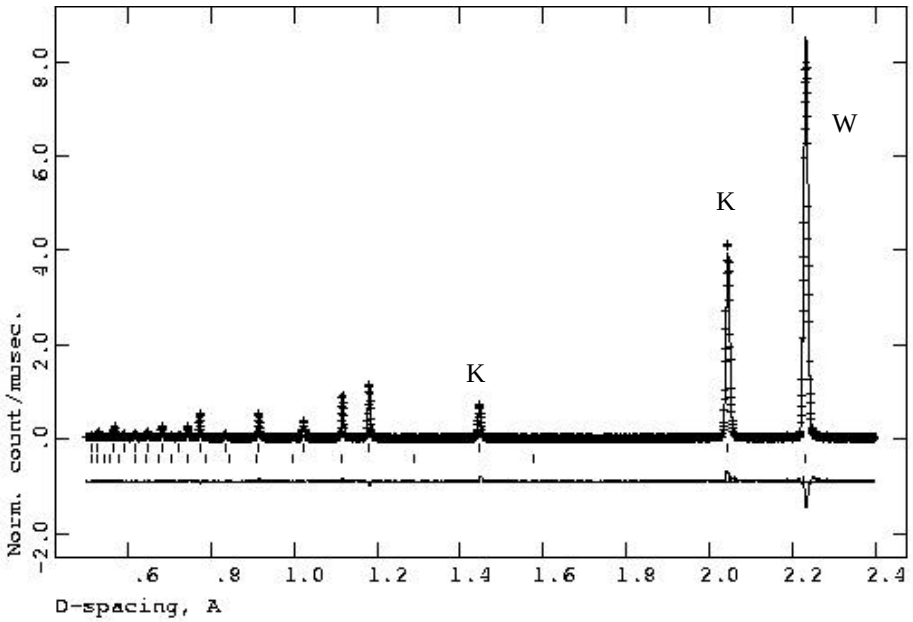


**(b)**

Figure 1: Diffraction Spectra for the 30 volume % tungsten fiber (W) reinforced Kanthal Matrix (K) composite in a) Q Perpendicular and b) Q Parallel to the fibers. Tick marks show calculated peak positions. The difference curve is shown beneath each spectrum (a fitted background has been subtracted from the data, and the intensity is normalized with respect to the incident spectrum).

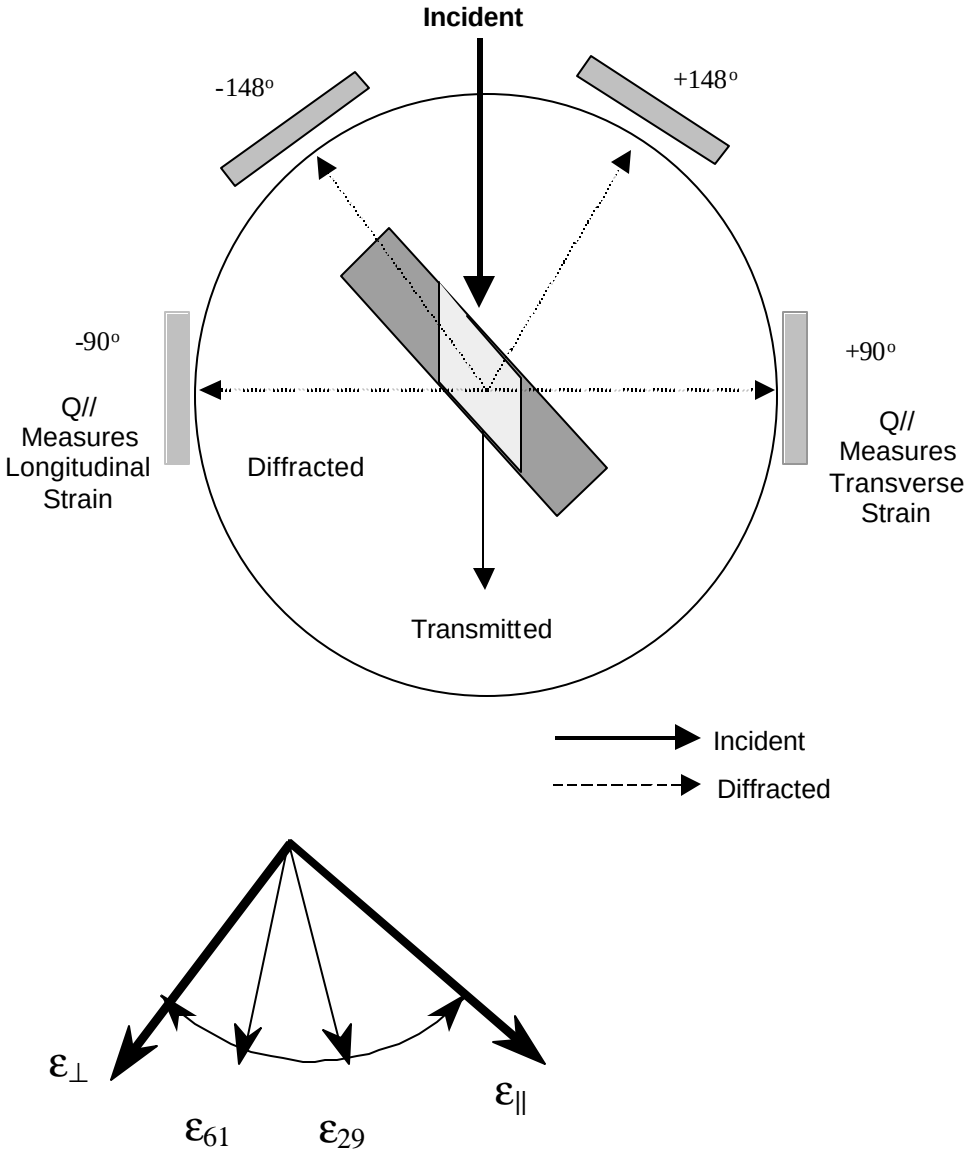


Figure 2. Sample orientation in the diffractometer (not to scale). The fiber axes are at 45° to the incident neutron beam. Four detectors are arranged around the sample. The +90° and –90° detectors measure strains perpendicular (Q⊥) and parallel (Q//) to the fiber axes respectively.

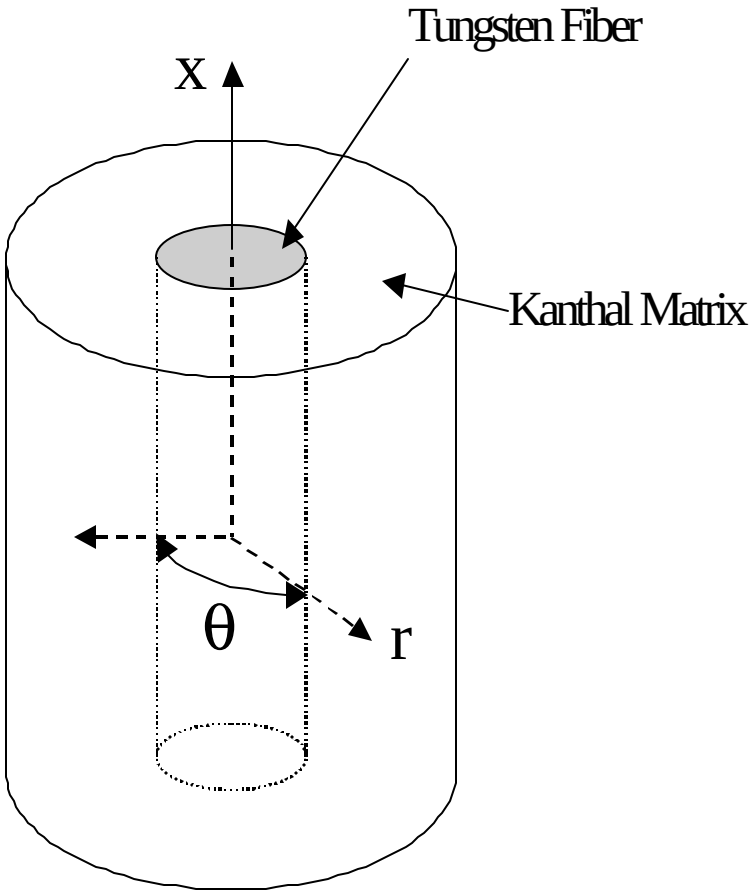


Figure 3: Geometry of the analytical concentric cylinder model (CCM).

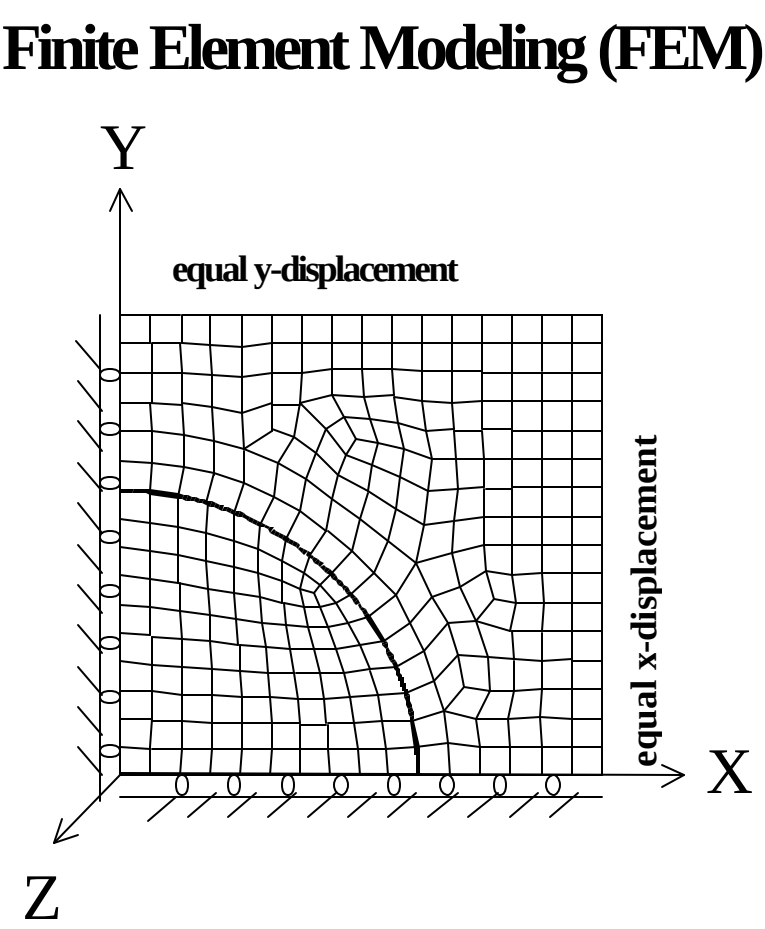


Figure 4: Finite Element Model mesh with boundary conditions ($V_f$ – 30%).

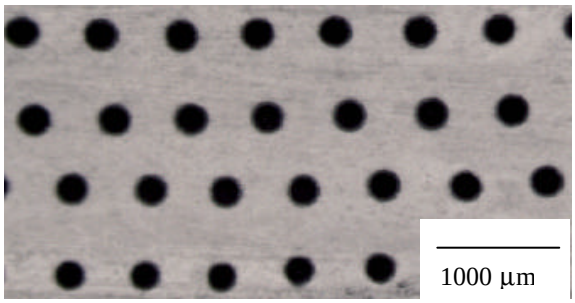


**(a)**

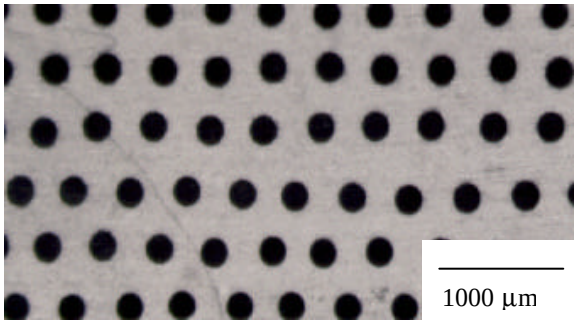


**(b)**

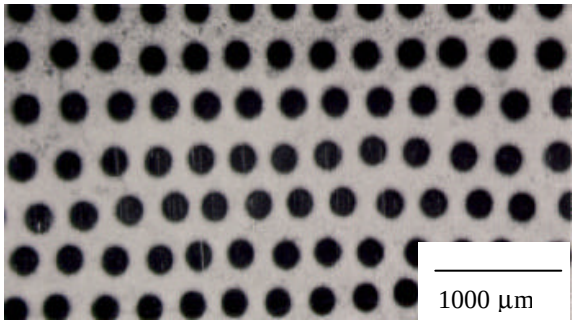


**(c)**

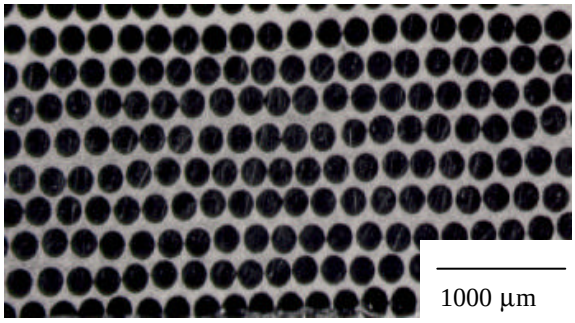


**(d)**

Figure 5. Optical micrographs (end view) of (a) 10, (b) 20, (c) 30, and (d) 70 % $V_f$ composite.

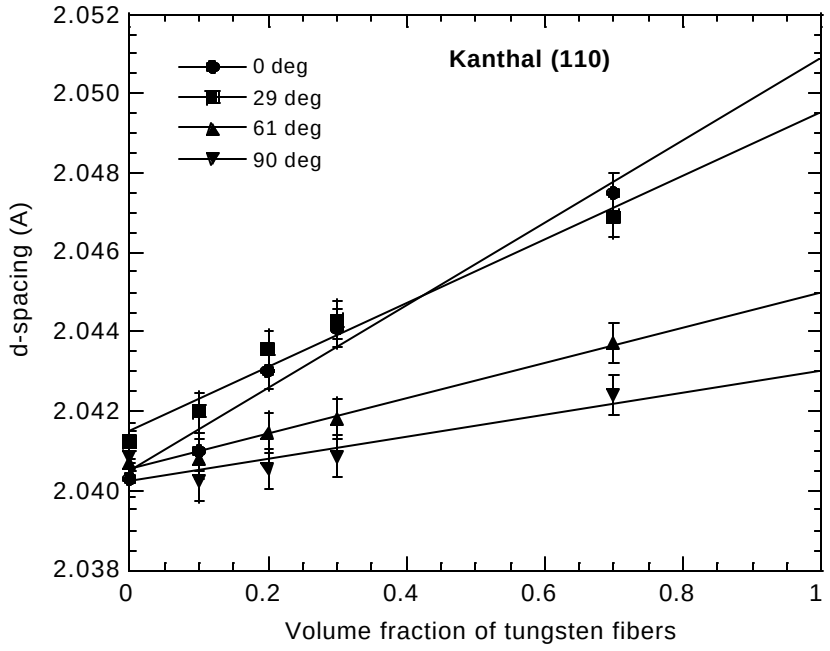


(a)

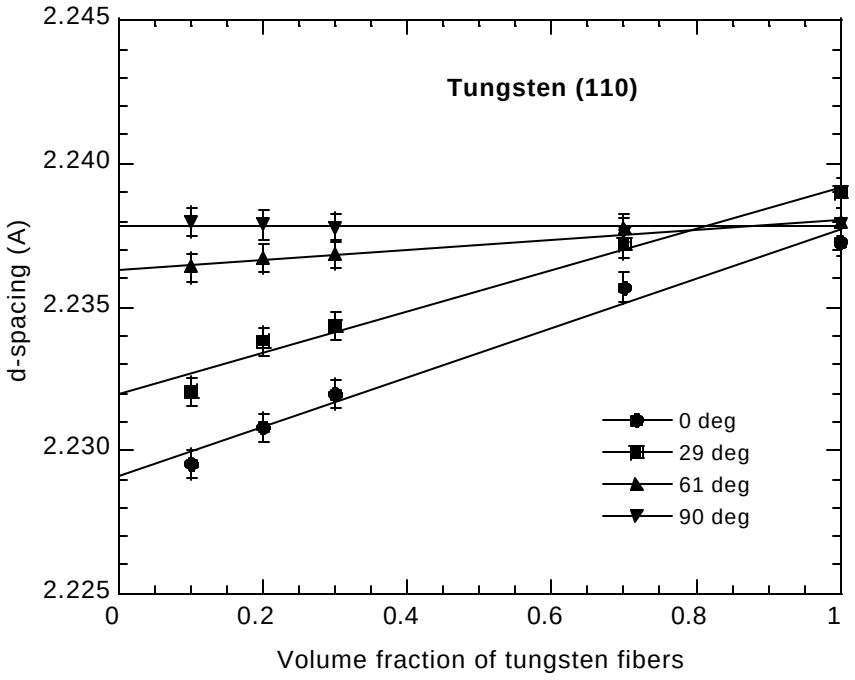


(b)

Figure 6: Measured d-spacing of Kanthal (top) and tungsten (bottom) versus fiber volume fraction.

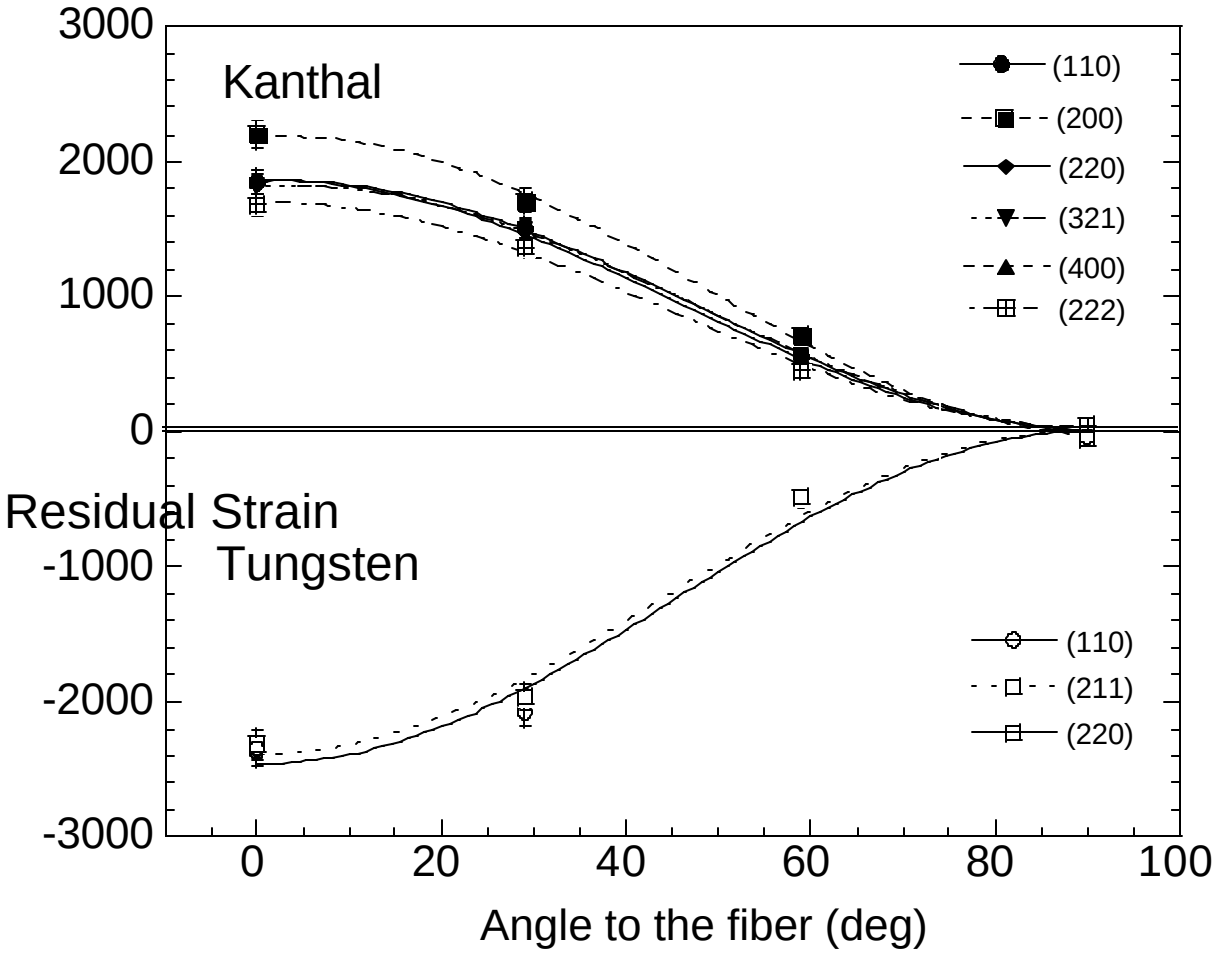


Figure 7: Measured plane specific (hkl) strains vs. angle to the fiber direction in the 30 vol. % W composite.

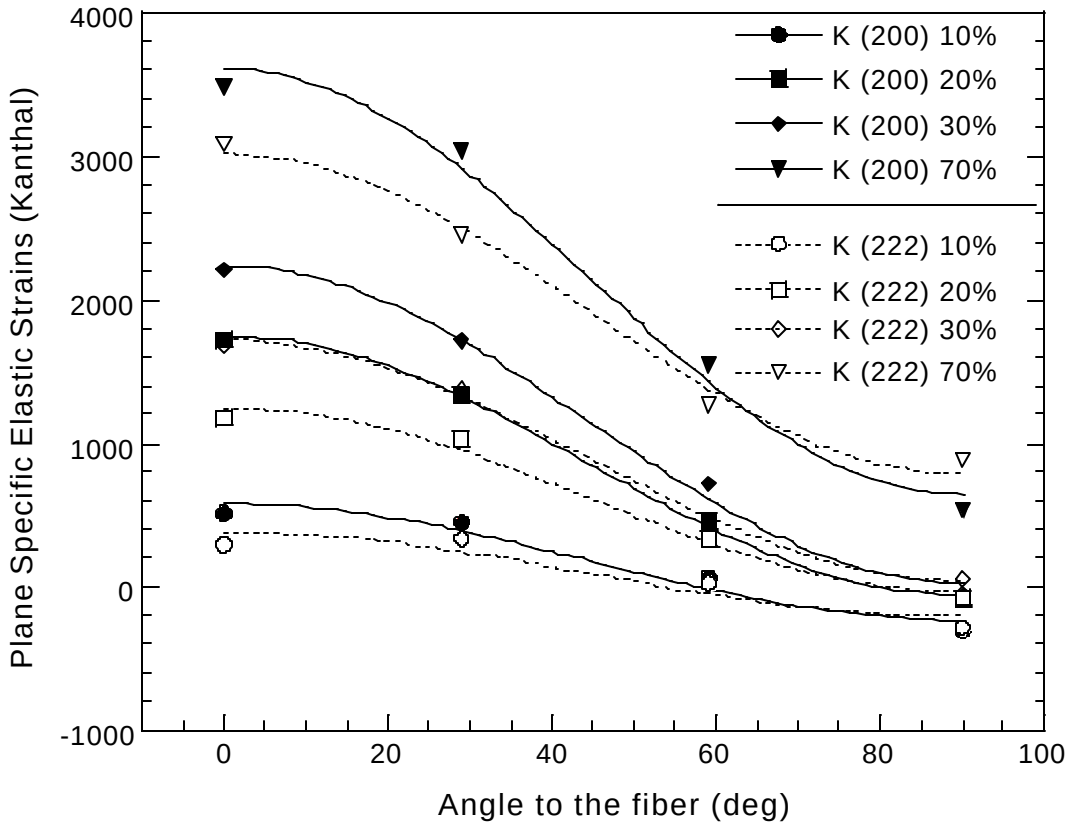


Figure 8a: Measured elastic strains for Kanthal 200 and 222 reflections (10, 20, 30 and 70 % $V_f$).

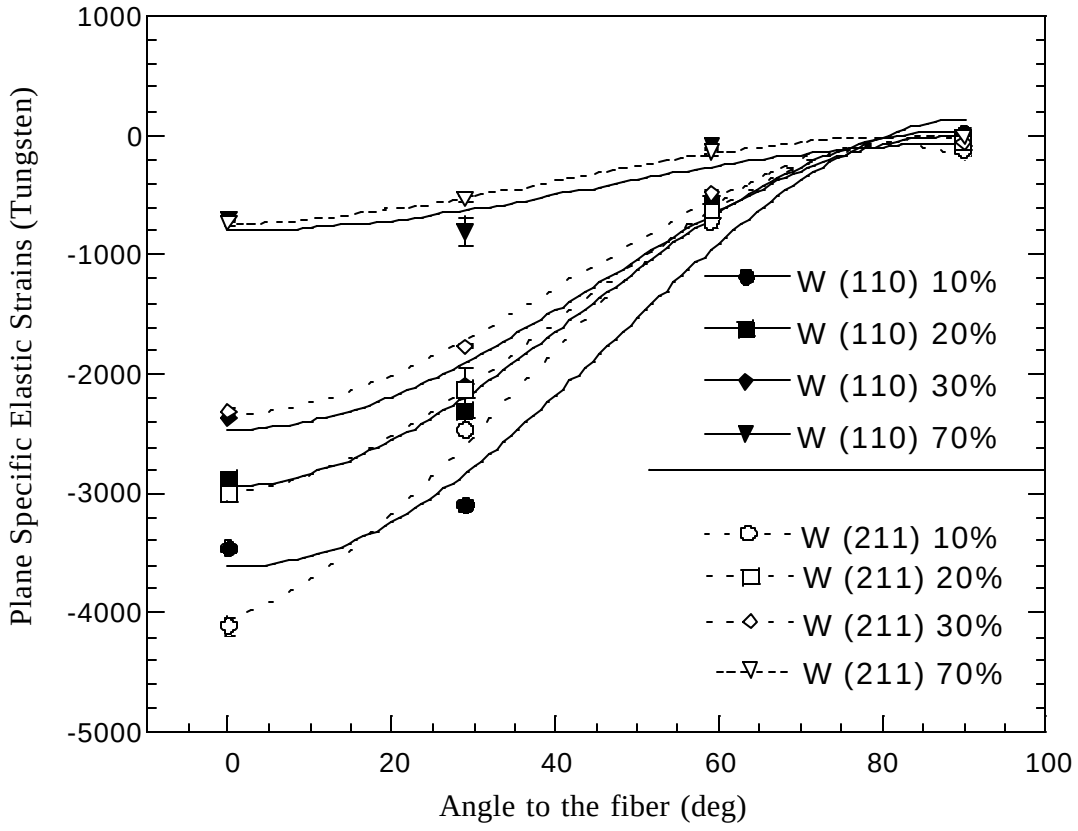


Figure 8b: Measured elastic strains for tungsten 110 and 211 reflections (10, 20, 30 and 70 % $V_f$).

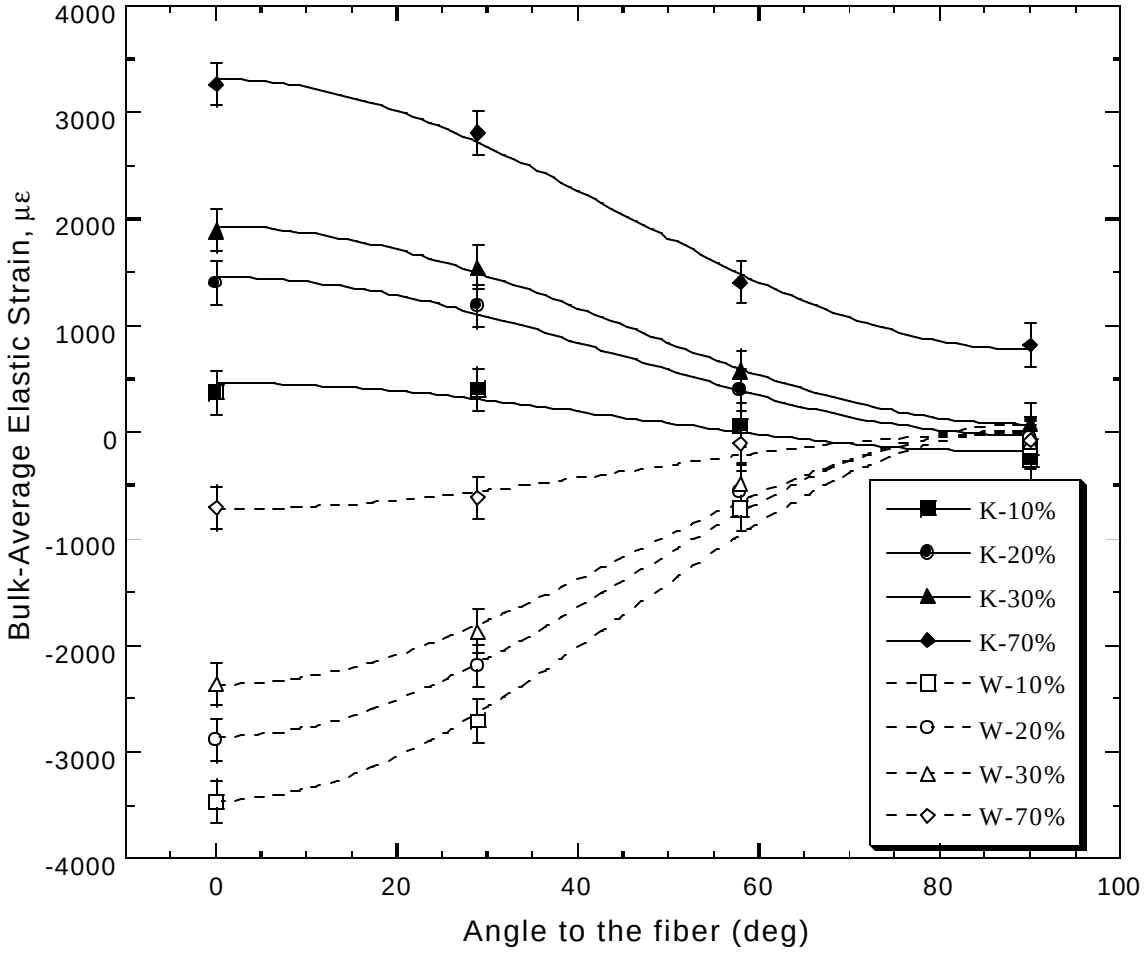


Figure 9: Measured mean phase (Rietveld) elastic strains vs. angle to fiber direction tungsten (10, 20, 30 and 70% $V_f$ )

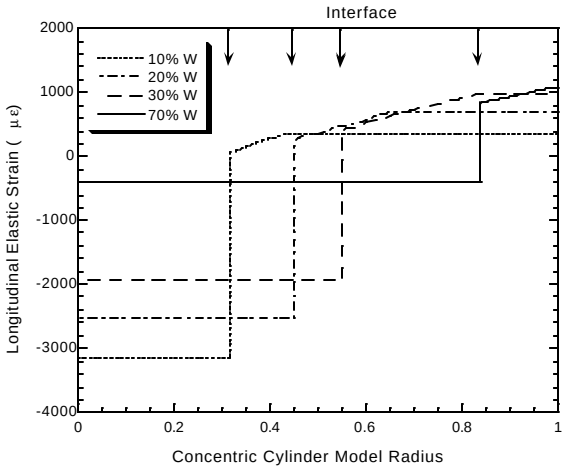


(A)

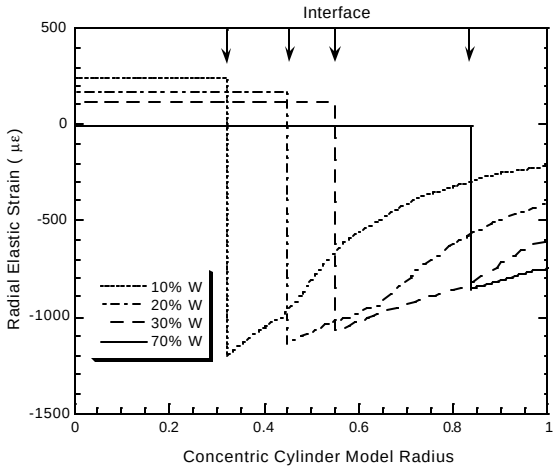


**(B)**

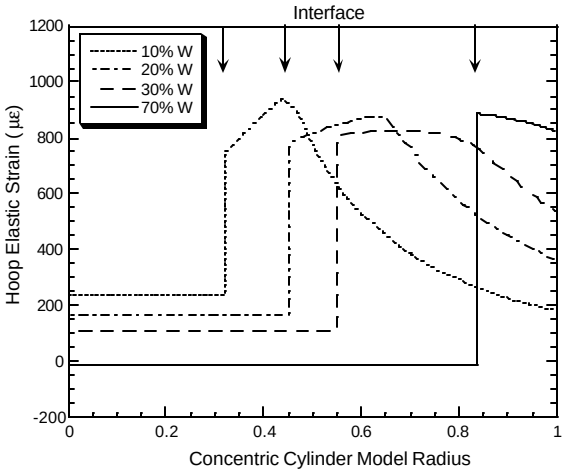


**(C)**

Figure 10: CCM Predictions of Longitudinal, Radial and Hoop Elastic Strains for 10,20,30 and 70 $V_f$ tungsten fiber composites.

## Elastic strains contour

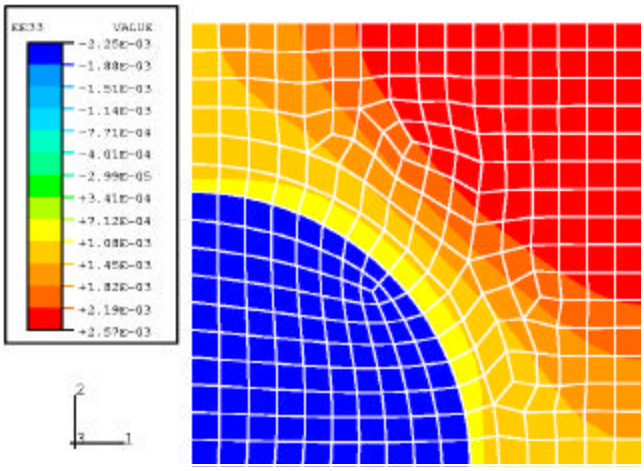


## Plastic strains contour

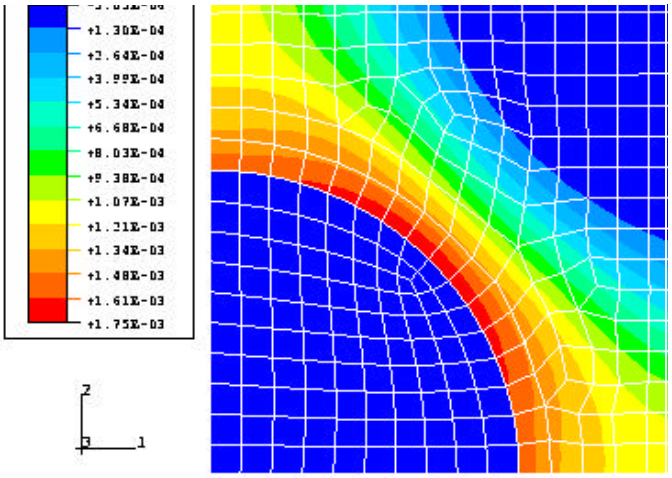


Figure 11: FEM elastic (upper) and plastic (lower) strain (με) contours in the longitudinal (parallel to the fiber) direction for a 30 $V_f$ tungsten fiber composite.

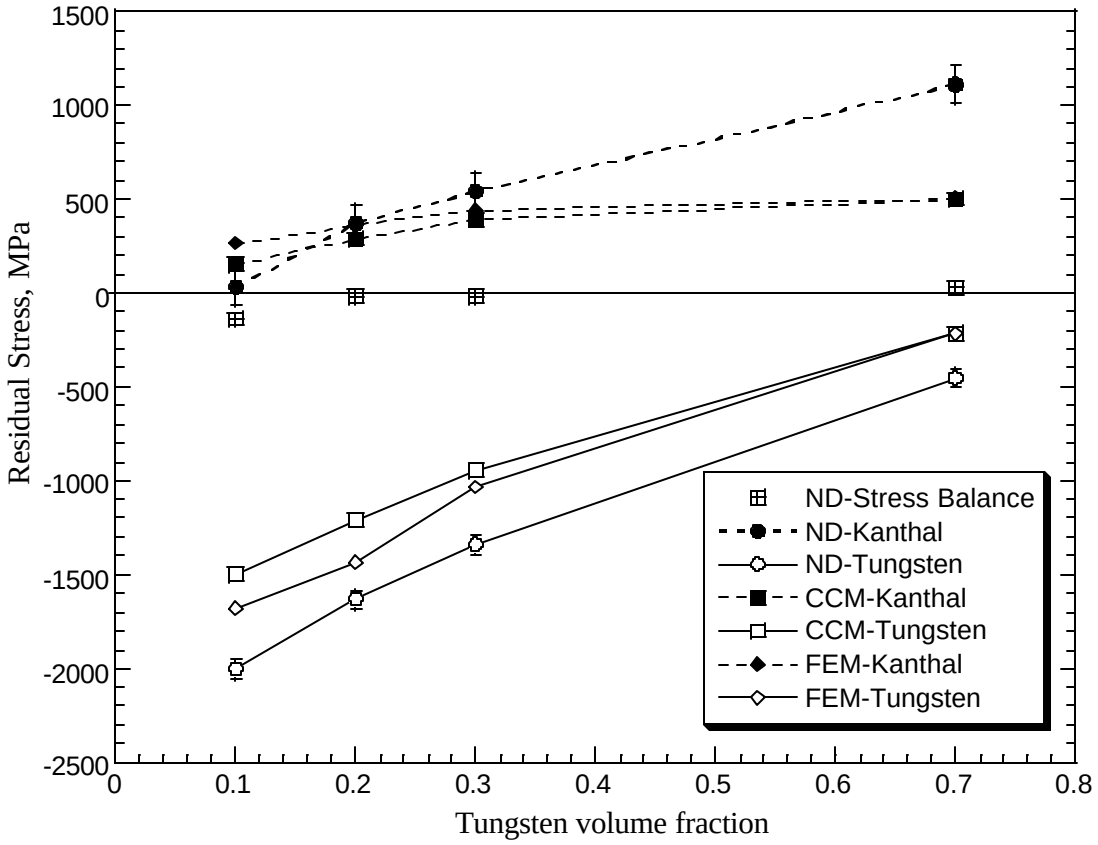


Figure 12: Longitudinal residual stresses vs. tungsten volume fraction (ND, CCM and FEM).

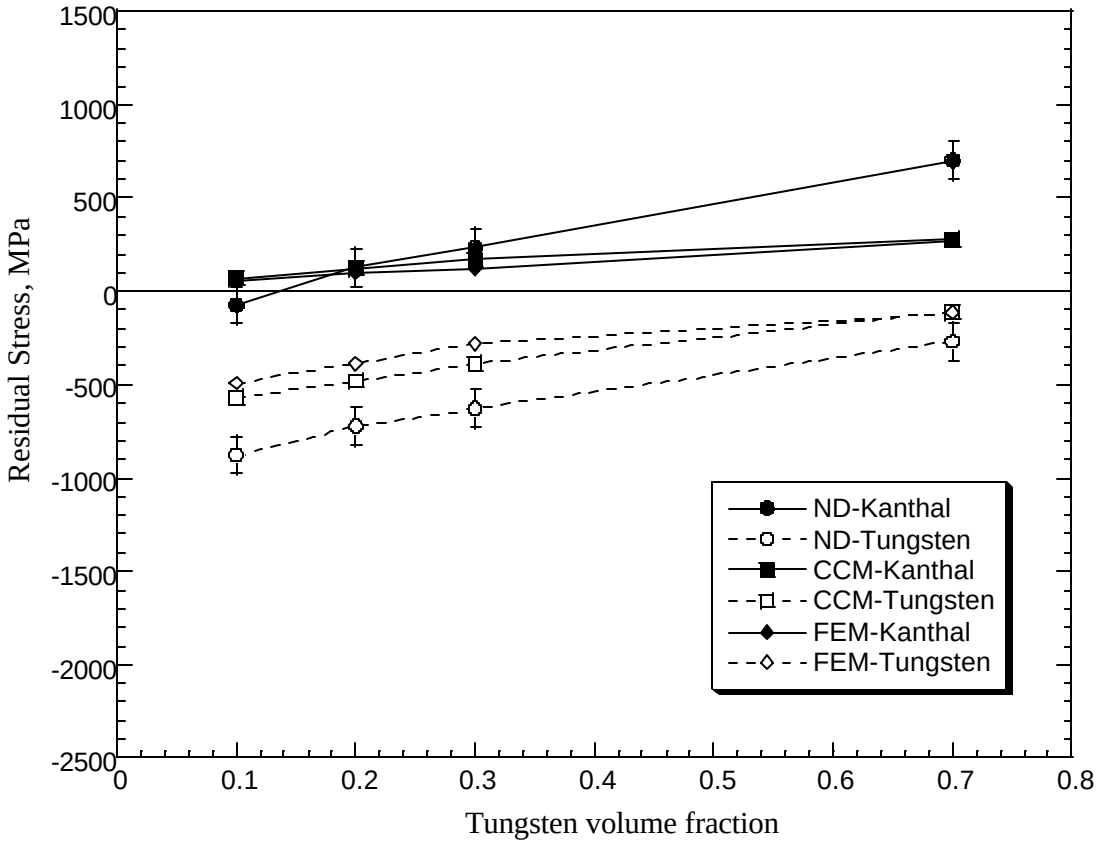


Figure 13: Transverse residual stresses vs. tungsten volume fraction (ND, CCM and FEM).

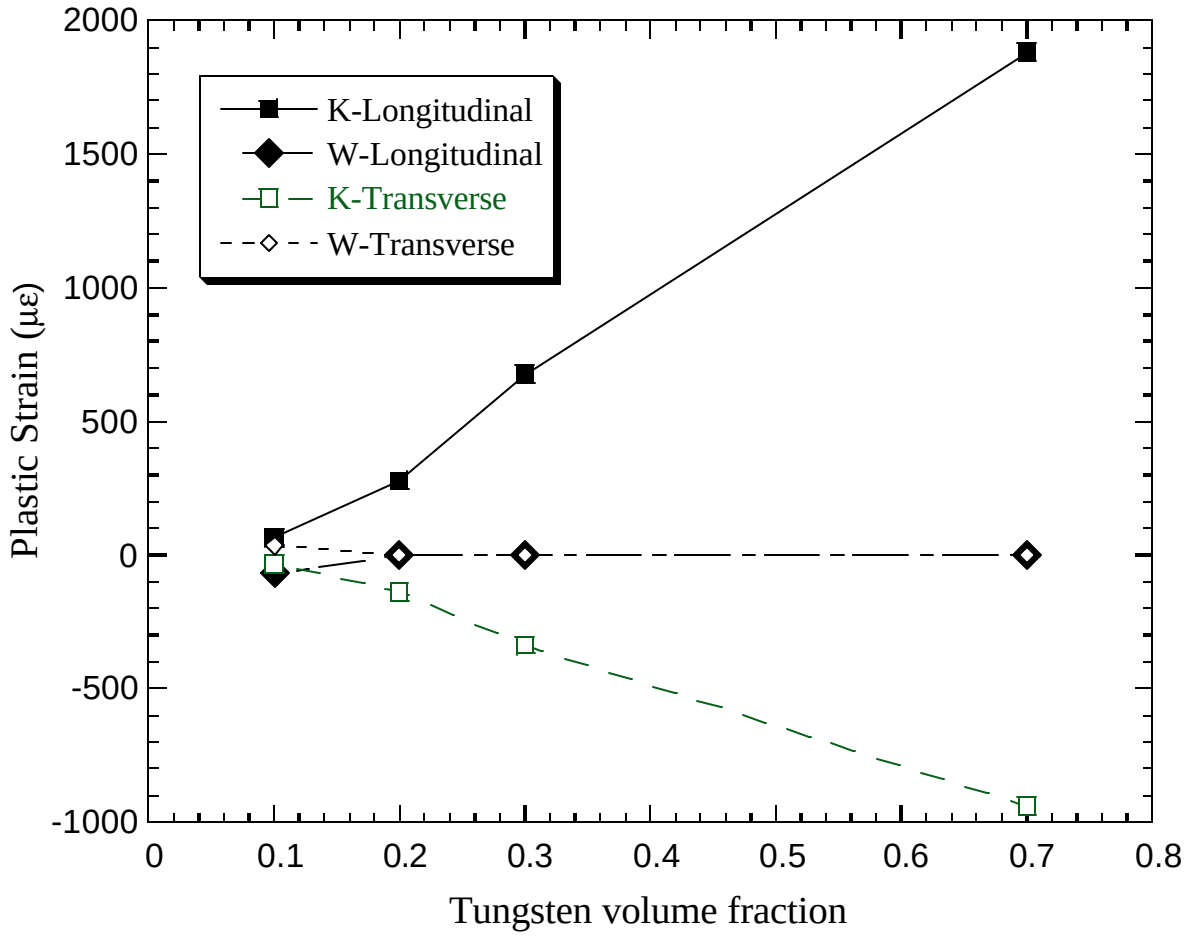


Figure 14: Volume averaged FEM plastic strains vs. volume fraction of tungsten fibers.